lubricants

MDPI

Article

Evolution of Microstructure, Hardness, and Wear Behavior of Medium-Entropy CuNiSiCrCoTiNbx Alloy

Denis Ariel Avila-Salgado [1,*], Arturo Juárez-Hernández [2,*], Nelson Javier Izaguirre-Bonilla [1], Jonathan Muñoz Tabora [3] and José Luis Camacho-Martínez [4]

[1] Departamento de Educación Tecnológica, Facultad de Tecnología (FATEC), Universidad Pedagógica Nacional Francisco Morazán, Colonia el Dorado, Tegucigalpa 04001, Honduras; nizaguirre@upnfm.edu.hn
[2] Facultad de Ingeniería Mecánica y Eléctrica (FIME), Universidad Autónoma de Nuevo León, Av. Universidad S/N, San Nicolás de los Garza 66450, Mexico
[3] Departamento de Ingeniería Eléctrica, Universidad Nacional Autónoma de Honduras, Boulevard Suyapa, Tegucigalpa 04001, Honduras; munoztabora@gmail.com
[4] Centro de Investigación en Ciencia Aplicada y Tecnología Avanzada, Instituto Politécnico Nacional, Unidad Querétaro, Querétaro 76090, Mexico; jolucenator@gmail.com
* Correspondence: denis.uanl.mx@hotmail.com (D.A.A.-S.); arturo.juarezhn@uanl.edu.mx (A.J.-H.); Tel.: +504-93820540 (D.A.A.-S.); +52-811-610-7184 (A.J.-H.)

Abstract: Medium-entropy alloys (MEAs) allow the formation of different phases, generally in a solid-solution state, and compounds that favor obtaining alloys with properties superior to those of conventional alloys. In this study, medium-entropy CuNiSiCrCoTiNbx alloys were fabricated via melting in a vacuum induction furnace. The influence of the Nb addition (X = 0, 0.5 and 1 wt%) alloying elements on the microstructure, hardness, and wear resistance of the $CuNiSiCrCoTiNb_0$ (M1), $CuNiSiCrCoTiNb_{0.5}$ (M2), and $CuNiCoCrSiTiNb_1$ (M3) alloys were explored using X-ray diffraction (XRD), scanning electron microscopy (SEM), and a ball-on-disc tribometer, respectively. In general, the results indicated that the incorporation of Nb alloying element promoted the evolution of the microstructure, increased the hardness, and improvement of the wear resistance. The XRD and SEM findings demonstrate that higher Nb addition and aging heat treatment (AT) modification mainly favored the formation of dendritic regions and the precipitation of the Co_2Nb, Cr_3Si, and Ni_2Si phases, which promoted the refinement and strengthening of the microstructure. Significant increases in hardness were recorded: 11.95% increased, promoted by the addition of Nb before (E1) and after (E2, E3, and E4) the heat treatments. The maximum hardness values recorded were 92 ± 0.11 (AC) and 103 ± 0.5 HRB (AT-60 min) for the M3 alloy. The increase in hardness caused by Nb addition and aging heat treatments contributed to the dry sliding wear resistance response, decreasing material loss by 20%. This was related to the high concentration of precipitated phases rich in CoNb, CrSi, and NiSi with high hardness. Finally, the M3 alloy aged for 60 min exhibited the best specific wear rate behavior, with a material loss of 1.29 mm^3. The commercial Cu-Be C17510 alloy experienced a maximum hardness of 83.47 Hardness Rockwell B, HRB, and a high wear rate of 3.34 mm^3.

Keywords: Cu-based alloys; medium-entropy alloys; Nb addition; microstructure; hardness; wear resistance

check for updates

Received: 27 February 2025
Revised: 1 April 2025
Accepted: 2 April 2025
Published: 5 April 2025

Citation: Avila-Salgado, D.A.; Juárez-Hernández, A.; Izaguirre-Bonilla, N.J.; Muñoz Tabora, J.; Camacho-Martínez, J.L. Evolution of Microstructure, Hardness, and Wear Behavior of Medium-Entropy CuNiSiCrCoTiNbx Alloy. *Lubricants* **2025**, *13*, 164. https://doi.org/10.3390/lubricants13040164

Copyright: © 2025 by the authors. Licensee MDPI, Basel, Switzerland. This article is an open access article distributed under the terms and conditions of the Creative Commons Attribution (CC BY) license (https://creativecommons.org/licenses/by/4.0/).

1. Introduction

1.1. General Considerations

Recent industrial and commercial expansion has driven the demand for metals with mechanical properties superior to those of conventional alloys. High-entropy alloys (HEAs), characterized by their multi-element composition, have demonstrated enhanced thermal stability, high hardness and strength, excellent ductility, and superior wear and corrosion resistance [1–3]. More recently, medium-entropy alloys (MEAs) have emerged as promising alternatives, exhibiting improved mechanical properties, reduced density, and, in some cases, enhanced corrosion resistance and thermal stability [4,5]. These attributes make MEAs highly suitable for critical applications in the automotive, aerospace, and power generation industries, prompting increased research efforts to optimize their composition, microstructure, and performance.

1.2. Literature Review

Recently, the number of studies aimed at enhancing metal strength has significantly increased, focusing mainly on elements with higher impact strength, such as alloys, to achieve higher wear resistance from the precipitated phases. As different alloys can provide these benefits, different metals and alloys have been studied using different application methodologies. This study proposes the implementation of medium entropy alloys to improve the wear resistance of materials.

To provide a structured approach to understanding the research landscape, a bibliometric and systematic methodology was applied, including (i) a structured literature search using the SCOPUS platform with predefined inclusion and exclusion criteria; (ii) bibliometric analysis to assess publication trends, geographic distribution, and institutional collaborations; (iii) keyword mapping via co-occurrence analysis in the VosViewer software 1.6.20 [6] to identify thematic connections; and (iv) content analysis to categorize the evolution of MEAs and their applications in wear resistance improvement. The identified trends and findings guided the discussion of the analyzed articles, ensuring a comprehensive evaluation of existing research.

This methodology started with a targeted bibliometric review performed on the SCOPUS platform using the following search terms “medium entropy alloy” AND “microstructure” AND “wear resistance”. Consequently, 206 scientific studies were identified, including research articles, conference papers, and book chapters.

Figure 1 shows a thematic map of the keywords extracted from the titles, abstracts, and keywords of the 206 studies analyzed using VOSviewer software [6]. The various relationships between keywords, such as medium entropy, microstructure, wear resistance, corrosion resistance, and alloys, can be seen in the thematic keyword map (Figure 1a). At medium entropy, alloys with Ni, Mn, Mo, Nb, and Ti are the most important connections. Studies on the defined keywords were also related to corrosion resistance, where sodium chloride, composite coatings, and silicon alloys were analyzed. In the microstructure cloud, terms such as tensile strength, crystal structure, properties, fracture toughness, friction, and others related to the composition of the materials appear with the goal of wear resistance.

In Figure 1b, the year of publication of the studies related to these keywords is presented, with the range between 2020 and 2024, which highlights the novelty of the topic addressed. Topics such as medium entropy, manganese alloys, nickel alloys, Brinell hardness, and tribological properties, among others, are addressed in 2024 and early 2025.

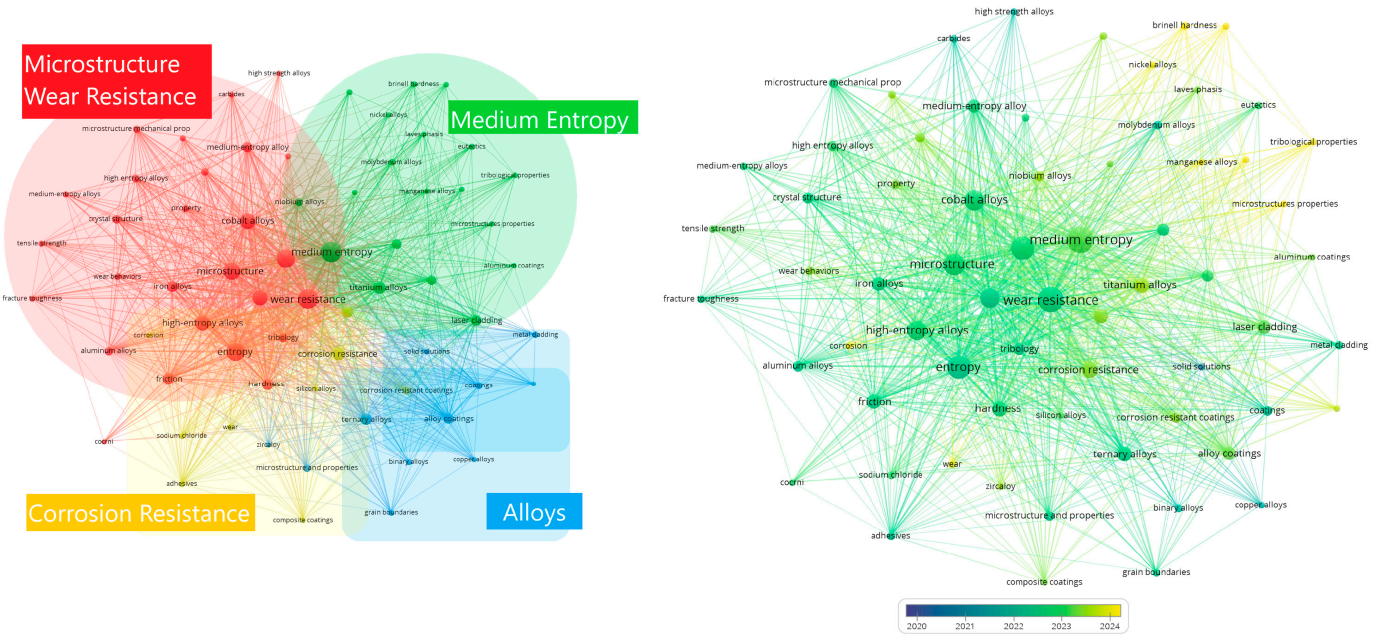

(**a**) (**b**)

Figure 1. Thematic map of keywords: (**a**) Keywords map separated by relevant categories; (**b**) medium-entropy alloys and methodologies used for 2020–2024 [6].

As shown in Figure 2, China, the United States, Hong Kong, and South Korea have led energy forecasting research. Japan, Taiwan, Canada, Germany, Australia, and India have completed the top ten countries with the most publications on this topic.

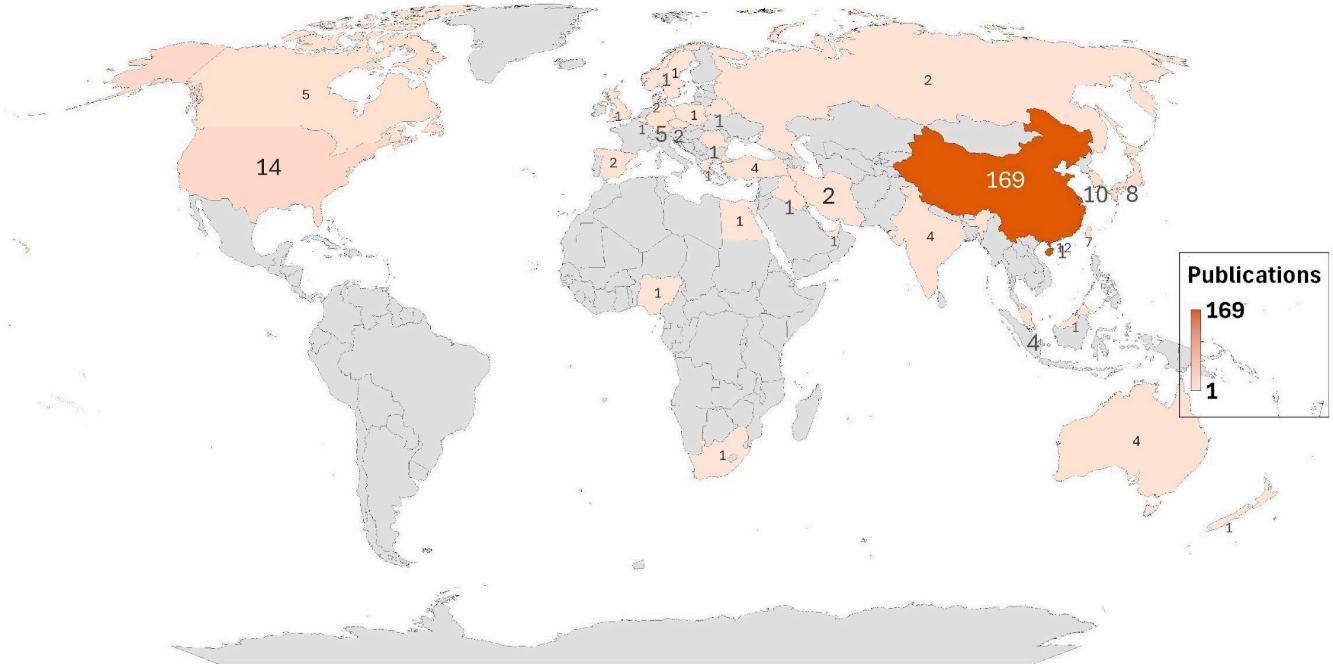

Figure 2. Distribution of publications related to medium-entropy worldwide [6].

From a global quantitative perspective, a survey of publications on mean entropy over the past decade was conducted, as seen in Figure 3a. The findings indicated that, since 2016, there has been a rise in the number of studies examining medium-entropy, with studies including new alloys in the search for higher wear resistance. In 2023, according to a survey,

the largest number of studies were conducted on mean entropy, microstructure, and wear resistance.

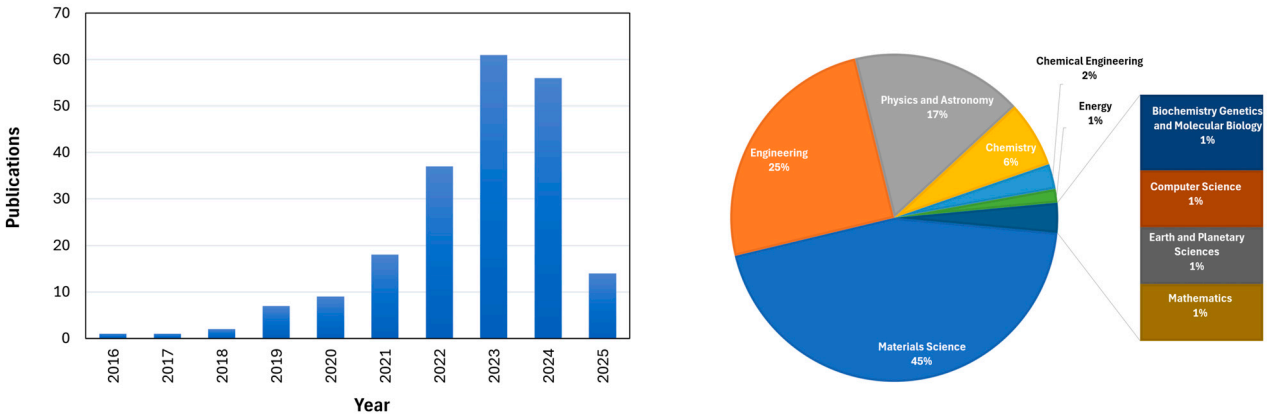

(**a**) (**b**)

Figure 3. Quantitative studies associated with medium-entropy: (**a**) Publications related to medium-entropy in recent years; (**b**) distribution of studies by subject area [6].

Of the total number of studies, 45% were in materials science, 25% in engineering, 17% in physics and astronomy, 6% in chemistry, and the remainder in other fields of study, as shown in Figure 3b, with 95% of the studies being of the article type.

The use of different alloys has become common in the industrial sector to optimize costs, improve product quality, and increase material versatility. In response to industrial demands, medium and high entropy alloys (MEAs and HEAs, respectively) have been extensively studied to improve their hardness, wear resistance, and thermal stability. Several studies have analyzed their microstructure, phase composition, and mechanical performance under various conditions.

Research on microstructural and mechanical behavior highlights key findings. The study in [7] examined coatings with varying Cu contents (Cu1.0, Cu0.7Al0.3, Cu0.5Al0.5, and Cu0.3Al0.7), with the aluminum adjusted accordingly to maintain x + y = 1. Meanwhile, a study in [8] focused on (CuNi)100-xCox alloys, showing that a higher Co content increases the strength (242 MPa to 384 MPa) but reduces ductility (15.5% to 1.9%) owing to the hardness of the (Ni, Co)-rich phase. The study in [4] also explored single-crystal NiCoCr MEAs, emphasizing the influence of crystallographic orientation on ductility and strain-hardening mechanisms.

Different alloy compositions have been investigated to improve the mechanical and wear resistance. A study in [9] showed that increasing the Hf content on the mechanical and tribological properties of CoCrNiHf alloys improves the hardness and wear resistance. Similarly, research in [10] indicated that Cr addition on the precipitation and properties of cryo-rolled CuNiSi alloys led to the formation of Cr_3Si particles that strengthened the material while maintaining electrical conductivity. In [11], a high-Fe aluminum alloy produced by additive manufacturing was studied to optimize its mechanical properties despite impurities, with promising results for sustainable industrial applications. The study in [12] examined TiC-reinforced metal matrix alloys, where ceramic reinforcement significantly improved wear resistance under high loads. Similarly, the research in [2] analyzed the effect of Cr_3C_2 in WC-CoNiFe alloys and showed that the hardness increased with Cr_3C_2 content, while the transverse rupture strength was optimized at intermediate concentrations. In addition, the study in [13] examined medium-entropy alloys, such as CrFeNi and CrFeNiB0.03Si0.03. This shows that the addition of B and Si improves hardness, reduces wear rate, and improves corrosion resistance.

Despite these advancements, improving wear resistance can sometimes compromise the corrosion performance, requiring a balance between mechanical durability and environmental stability. The study in [14] highlights how optimizing wear resistance in CoNiCrMo MEAs may reduce corrosion resistance, highlighting the importance of balancing mechanical properties and corrosion resistance. However, other studies have suggested that high-Cut HEAs can provide superior corrosion protection. Research in [15–17] indicates that Cu ion release inhibits marine biofilm formation and enhances antibacterial properties, with an antibacterial rate against *E. coli* reaching 97% when x = 0.2 and about 90% when x = 0.3. The wear and corrosion resistances were improved at [13] by incorporating B and Si into CrFeNi alloys. CrFeNiB 0.03 Si 0.03 alloy was used, which has twice the microhardness (403 HV 0.2) and a 40% reduction in wear rate compared to CrFeNi MEA. In addition, this alloy showed improved corrosion resistance in NaCl solutions and formed denser and more protective passivation films. Each article offers a unique approach to address corrosion resistance through composition optimization, specific alloy design, or surface modification.

1.3. Motivation and Contributions

The development of new alloys with superior mechanical properties is critical for industrial applications that require high strength, durability, and structural stability. In this context, copper-based medium-entropy alloys (MEAs) have emerged as promising alternatives to commercial alloys, such as CuBe C17510, owing to their ability to form solid solutions and stable crystal structures, as well as their potential for improved hardness and wear resistance. However, the influence of strategic alloying elements, such as Nb, and specific heat treatments on the microstructure and mechanical performance of these alloys still requires detailed investigation. This work investigates the effect of Nb addition and heat treatment on the phase transformation, structural properties, material strength, and durability of copper-based medium entropy alloys (MEAs) compared to the commercial alloy CuBe C17510. To this end, the following objectives are proposed:

- Evolution of configurational entropy as a function of Nb content and its influence on phase stability and solid solution formation of BCC and FCC structures.
- The microstructure of the alloys was characterized by XRD and SEM-EDS to identify the crystalline phases and evaluate the effect of Nb on the lattice parameters.
- To analyze how Nb and different heat treatments influence the refinement and distribution of the precipitated phases and the evolution of the hardness of the alloys in the cast and aged states.
- To determine the wear behavior of the MEA under different heat treatment conditions, they were compared with the CuBe C17510 alloy to establish their viability in applications where wear resistance is a key factor.

2. Materials and Methods

Medium entropy CuNiSiSiCrCoTiNb0 (M1), CuNiSiCrCoTiNb0.5 (M2), and CuNiSiCrCoTiNb1 (M3) alloys (MEAs) were obtained by a melting process using a 5 kg capacity CONSARC vacuum induction furnace (made in the USA) at a temperature of 1300 °C under a protective argon atmosphere. The molten metal was poured into rectangular H13 steel molds. The materials used in this study were Cu, Ni, Co, Cr, and Si of high purity (99.99% pure). Ti (73Ti-4.7Al-22.3Fe) and Nb (65Nb-32Fe-3Si) were added as ferroalloys (supplied by Marco Metales de México, S. De R.L. De C.V., Apodaca, México). The chemical compositions and alloy identifications are listed in Table 1. Rectangular ingots, weighing 5 kg, were used. After casting, the alloys were analyzed for their chemical compositions. The samples were analyzed using X-ray fluorescence spectroscopy. After casting, pouring,

and cooling the ingots of each alloy, square samples of 20 × 20 × 10 mm square samples were cut using a La-bottom-5 cutting machine with a cooling system.

Table 1. Nominal chemical compositions of MEAs.

	C				Elemental Constituents (wt%)			
Alloy	**Cu**	**Ni**	**Si**	**Cr**	**Co**	**Ti**	**Fe**	**Nb**
M1	79.90	5.50	5.50	5.50	1.00	2.00	0.60	0.00
M2	79.13	5.50	5.50	5.50	1.00	2.00	0.87	0.50
M3	78.39	5.50	5.50	5.50	1.00	2.00	1.11	1.00

Once the samples of each alloy were cut, we proceeded to identify as E1 the sample in the casting condition (AC), E2 with solubilized heat treatment (ST) at 900 °C in a room atmosphere for 1 h with cooling in water at room temperature, and E3 and E4 modified with aged heat treatment (AT) at 500 °C for 30 and 60 min, respectively, with cooling at room temperature. A Felisa electric furnace was used to perform the heat treatment.

For microstructural analysis, hardness, and wear, samples E1, E2, E3, and E4 were superficially ground with silicon carbide abrasive paper up to grit 4000 until a mirror-like surface was obtained.

For each phase analysis, square specimens with dimensions of 10 × 10 × 3 mm were prepared. The samples obtained before and after thermal treatment were superficially polished until a mirror-like surface was obtained. The study used an X-ray diffraction (XRD) apparatus with a monochromatic Co Kα1 radiation source (wavelength = 1.7890 Å), operated at 40 KV and 40 mA in a 2θ range of 20° to 120°.

In addition, the microstructure and chemical composition of the phases were determined by optical microscopy (O.M.) and scanning electron microscopy (SEM) using a Jeol model JSM 6510LV microscope (Jeol Ltd., Akishima, Tokyo, Japan) equipped with EDS, which was operated in the secondary and backscattered electron mode at an accelerating voltage of 20 kV. Rockwell B and Vickers hardness measurements were performed using a Rockwell TH 320-INCOR digital hardness tester (Mituto-yo Corporation Ltd., Kawasaki, Kanagawa, Japan), which performed 15 indentations on each specimen with an applied load of 980 N for 10 s, and a Vickers model 402 MVD hardness tester, which applied a load of 0.025 N for 15 s.

Finally, the friction and wear behaviors were analyzed through a ball-on-disc tribometer (Ball-on-Disc Wear Testing Machine, UANL, Monterrey, Nuevo León, Mexico) with a normal load of 30 N under a dry sliding condition at room temperature. A G25 stainless steel ball with a diameter of 11.1 mm was used for the test, according to ASTM-G99-95 [18]. The experimental setup included an initial footprint radius of 6 mm and sliding speed of 365 rpm for 500 m, with wear track measurements of 125 m, 250 m, 375 m, and 500 m. The wear track and material loss (mm^3) were analyzed using a non-contact optical profilometer (NANOVEA PS50 3D, Irvine, CA, USA). To ensure the accuracy of the results, the test was performed in duplicate for each sample condition to obtain reliable and repeatable results. SEM-EDS was used to examine the morphology and chemical composition of the abraded surfaces.

3. Considerations of Thermodynamic Properties in the Formation of Phases in MEAs

The formation of phases and compounds is mainly governed by different thermodynamic parameters and Gibbs energy differences, which affect the entropy and enthalpy changes in the system. On the other hand, phases in solid solutions and intermetallic com-

pounds experience significant increases in configurational entropy (ΔS_{Conf}) with values between $12 \leq \Delta S_{Conf} \leq 17.5$ J/mol.K, which is conducive to the phase stability at high temperatures [19]. Furthermore, Guo and Liu demonstrated that the formation of solid solutions is possible as long as the values of ΔS_{Conf}, ΔH_{Mix}, and δ are in the range between $11 \leq \Delta S_{Conf} \leq 19.5$ J/mol.K, $-22 \leq \Delta H_{Mix} \leq 7$ KJ/mol, and $\delta \leq 8.5\%$ [20].

In the present work, it was found that the values of ΔS_{Conf} and ΔH_{Mix} are within the range that favors the formation of solid solutions; evidently, the high probability of formation is for the Nb-containing alloys because their configurational entropy value increases gradually.

Jointly, the parameter Ω is related to the ΔH_{Mix} y ΔS_{Conf} to predict the possible stability of solid solutions; such stability will be possible if the values of omega (Ω) and atomic size difference (δ) are expressed as follows $\Omega \geq 1.1$ and $\delta \leq 6.6$ [21].

On the other hand, Guo et al. report that the stability of BCC- and FCC-type phases is also directly affected by the valence electron concentration (VEC), stating that BCC- and FCC-type structures are stable at a VEC of <6.87 and ≥8, respectively [22]. Overall, the electronegativity difference (Δχ) should be between $0.11 \leq \Delta\chi \leq 0.17$ [23]. The calculations and values obtained in this work predict that the M1, M2, and M3 alloys will be composed of FCC and BCC-type phases.

Therefore, for the design of the medium entropy CuNiSiCrCoTiNbx alloy system in this study, calculation and analysis of the main thermodynamic criteria that directly influence the possible formation of solid solutions and structures of the BCC and FCC types were performed, and the requirements with the highest relevance can be summarized as follows.

The thermodynamic values of the mixing enthalpy (ΔH_{Mix}), configurational entropy (ΔS_{Conf}), atomic size difference (δ), electronegativity difference (Δχ), valence electron concentration (VEC), omega (Ω), and melting temperature of the mixture (Tm) are important for predicting the possible of solid solutions formation crystalline structures, and intermetallic compounds. The above parameters were obtained using Equations (1)–(6), and the results are presented in Table 2.

$$\Delta H_{Mix} = \sum_{i=1,\ j\neq i}^{n} 4\Delta H_{ij} C_i C_j \quad (1)$$

$$\Delta S_{Conf} = -R\sum_{i=1}^{n} C_i ln C_i \quad (2)$$

$$\delta = \sqrt{\sum_{i=1}^{n} C_i\left(1-\frac{r_i}{\bar{r}}\right)^2},\ \bar{r} = \sum_{i=1}^{n} C_i r_i \quad (3)$$

$$\Delta\chi = \sqrt{\sum_{i=1}^{n} C_i(\chi_i - \bar{\chi})^2},\ \bar{\chi} = \sum_{i=1}^{n} C_i\chi_i \quad (4)$$

$$\mathrm{VEC} = \sum_{i=1}^{n} C_i(VEC)_i \quad (5)$$

$$\Omega = \frac{T_m\ \Delta S_{conf}}{|\Delta H_{Mix}|},\ T_m = \sum_{i=1}^{n} C_i(T_m)_i \quad (6)$$

where R is Boltzmann's constant (8.3145 J/K-mol); C_i y C_j is the atomic concentration of the ith and jth atoms; ΔH_{ij} is the binary mixing enthalpy AB for alloys of different components; T_m is the theoretical melting temperature of the mixture; r_i is the atomic radius of each element; and χ_i is the Pauling electronegativity of each element.

Table 2. Thermodynamic parameters for phase formation in MEAs.

Alloy	Phase	ΔH_{Mix} (k·J/mol)	ΔS_{Conf} (J/mol·K)	δ (%)	Δχ (%)	VEC	Ω	Tm (K)
M1	FCC/BCC	−7.14	8.11	5.44	0.110	8.93	1.68	1483.15
M2	FCC/BCC	−7.16	8.38	4.05	0.080	9.61	1.69	1488.15
M3	FCC/BCC	−7.17	8.61	4.11	0.082	9.58	1.79	1494.15

4. Results and Discussion

4.1. The XRD Patterns Prior to Heat Treatment

Figure 4 shows the XRD patterns of the medium entropy alloys (MEAs) in the as-cast state (E1). Figure 4a shows the X-ray spectra in the 2θ range from 40° to 125°, while Figure 4b shows an enlargement of Figure 4a in the 2θ range from 48° to 55°, allowing a detailed analysis of the (111) peak. In Figure 4a, it can be seen that alloys M1, M2, and M3 have mainly FCC phases (αCu) and precipitated phases (Co_2Nb, Cr_3Si and Ni_2Si). It can also be seen that alloys M2 and M3 have high intentionality in the diffraction peak (111) [see Figure 4b]. This effect can be attributed to the preferential orientation of the Cu-rich matrix in the crystallographic direction. In addition, Figure 4b shows that the (111) peak underwent a significant change in the diffraction angle, with a slight shift to a larger angle from 50.64°, 50.65°, and 50.69° as the content of Nb increased. This behavior, linked to the addition of Nb, which causes the lattice parameter constant to decrease from 3.623 Å for the M1 alloy to 3.622 Å for M2 and 3.620 Å for M3. These lattice parameter values were calculated from the XRD results using Equations (7)–(9).

$$2d\sin\theta = \lambda \tag{7}$$

$$d = a/\sqrt{h^2 + k^2 + l^2} \tag{8}$$

$$a = \lambda\sqrt{h^2 + k^2 + l^2}/(2\sin\theta), \tag{9}$$

where d is the interplanar distance of the crystal; θ is the diffraction angle; λ is the X-ray diffraction wavelength of Co Kα1 (λ = 1.7890 Å); a is the lattice constant; and *h*, *k*, and *l* are the Miller indices of the crystal.

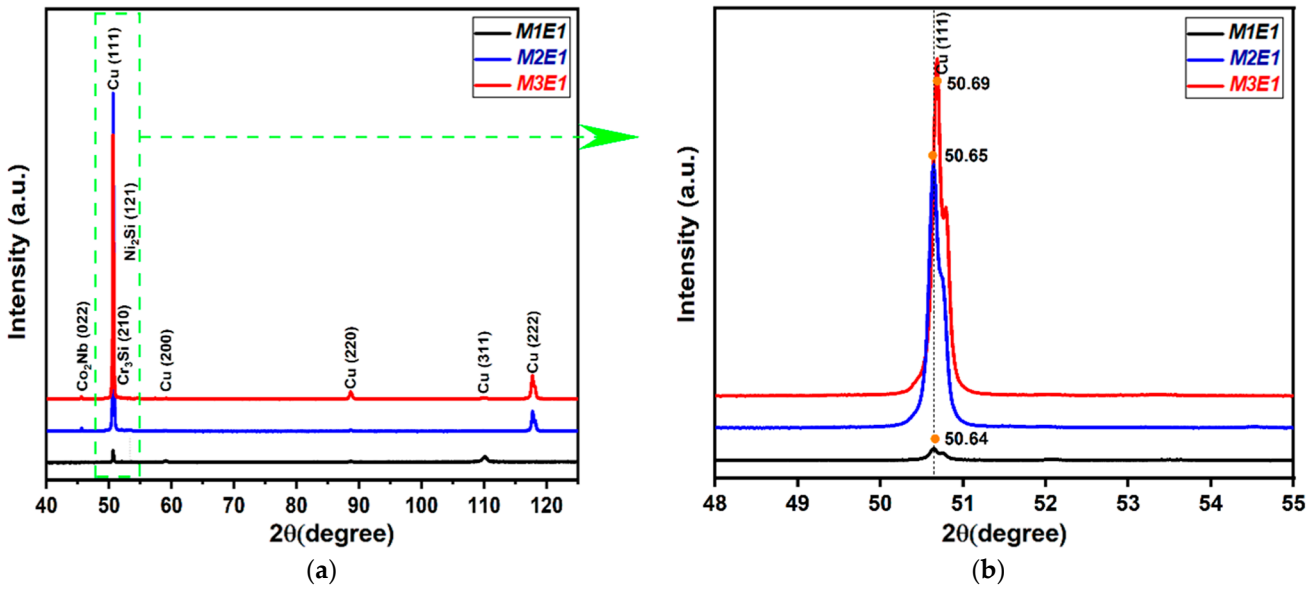

Figure 4. XRD patterns of the MEAs: (**a**) M1, M2, and M3 alloy in as-cast condition (E1); (**b**) some enlarged peaks of (**a**).

4.2. Microstructural Characterization Before Heat Treatments

Microstructural analysis of medium entropy alloys (MEAs) was carried out using an optical microscope to observe the effect of the addition of Nb. The samples studied were prepared using conventional metallographic techniques, followed by a chemical attack consisting of a solution containing 3.3 g of $FeCl_3$ in 100 mL of ethanol plus 17 mL of HCl and 1 mL of HNO_3. The samples were immersed for a period of 1 to 5 s, rapidly rinsed with water at room temperature, and dried with compressed air [24].

The cast microstructures shown in Figure 5 correspond to alloys M1, M2, and M3. Dendritic and interdendritic structures were observed in all alloys. All the alloys showed a dendritic structure composed of three phases, designated A, B, and C. The αCu-rich matrix is associated with the p hase A, which showed a decrease in its volume content with increasing Nb incorporation in alloys M2 and M3. Reducing the αCu-rich phase A increases the NiSiTi and CrSi-rich phases B and C, respectively. Moreover, the B phase is found at the margins of the dendritic arms of the C phase. By comparing Figure 5a–c, it is also possible to distinguish a gradual refinement effect in the microstructure owing to increasing Nb addition. Nb addition refines the microstructure, which is favorable for improving properties such as hardness and wear resistance.

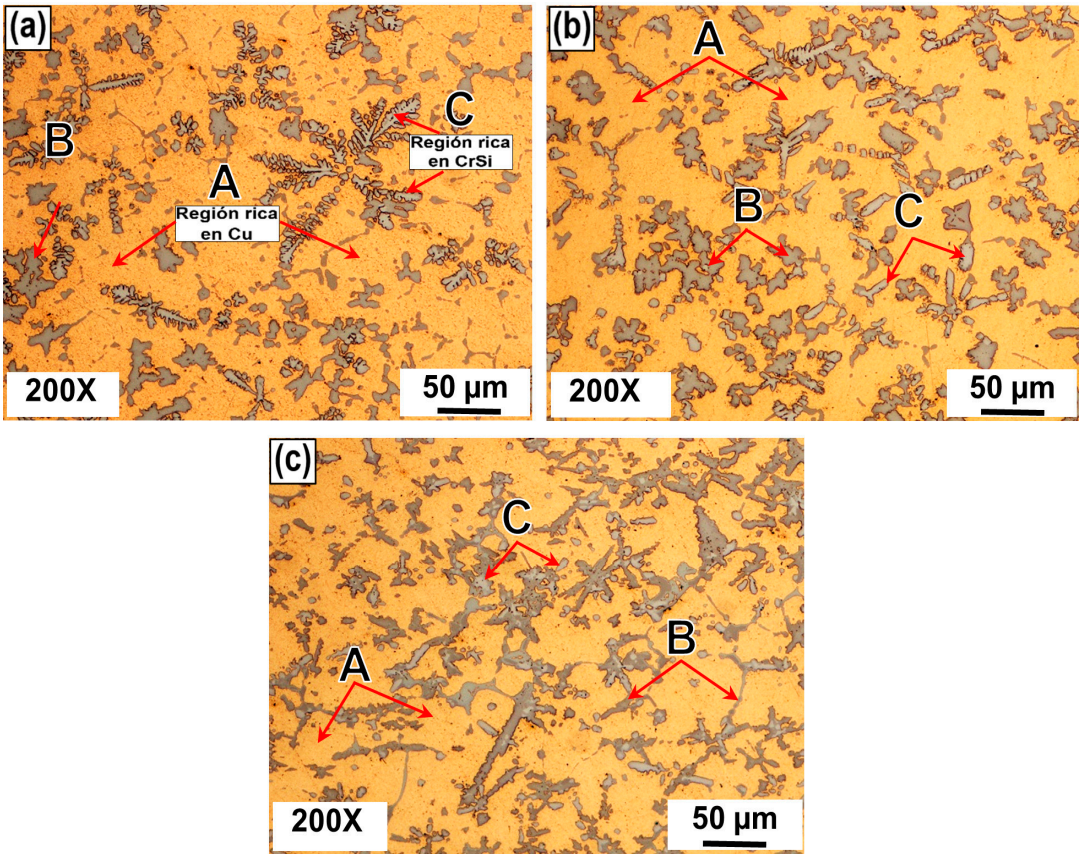

Figure 5. Optical micrographs of MEAs in as-cast condition: (**a**) M1E1, (**b**) M2E1, and (**c**) M3E1.

4.3. XRD Patterns Following Heat Treatments

Figure 6 shows the XRD patterns used to examine the effect of heat treatment on alloys (a) M1, (b) M2, and (c) M3. A magnified view of the prominent peaks in Figure 6c is shown in Figure 6d. It is important to note that all alloys contain the FCC/BCC phase and precipitated phases, such as Co_2Nb, N_2Si, and Cr_3Si.

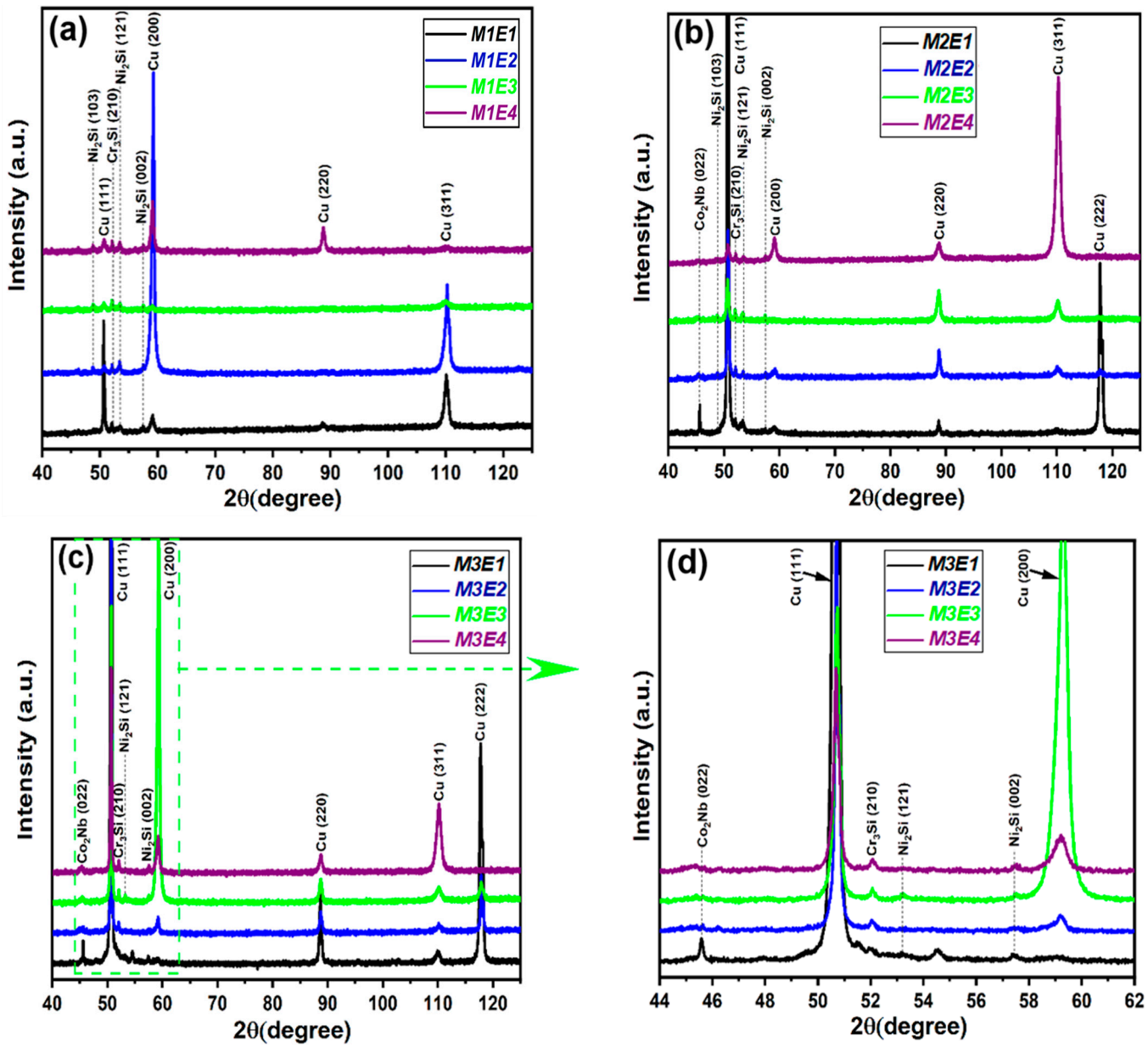

Figure 6. XRD patterns of MEAs: (**a**) M1, (**b**) M2, and (**c**) M3 alloy before (E1) and after heat treatments (E2, E3, E4); and (**d**) the enlarged peaks of (**c**).

Figure 6a also shows a significant decrease in the intensity of the main (111) peak, indicating that the AT-30 and AT-60 aging heat treatments promoted microstructural evolution and tended to facilitate the formation of precipitated phases. In addition, the solubilizing heat treatment (ST) caused a high intensity in the diffraction peak (200), corresponding to the αCu phase. Similarly, in Figure 6a–c, it can be observed that the diffractograms for samples E3 and E4 experience low intensity in most of the diffraction peaks, which is consistent with the evolution of the microstructure and strengthening of the properties.

4.4. Microstructure Analysis by SEM

Figure 7a presents a sequence of SEM images in the secondary electron mode (SEI) of the M3 alloy in the as-cast state (E1) and after heat treatments as ST (E2), AT-30 (E3), and (E4) AT-60. In this case, the microstructures also evidence three different colored phases: the light-gray regions are labeled A, the dark-gray regions are labeled B, and the black regions are labeled C. A, B, and C represent the phases present in the microstructures.

As can be seen again when comparing Figure 7a, a higher content of αCu-FCC phase A and NiSiTi-rich dendritic phase B, as well as a lesser amount of CrSi-rich phase C were observed; these were measured in the next section.

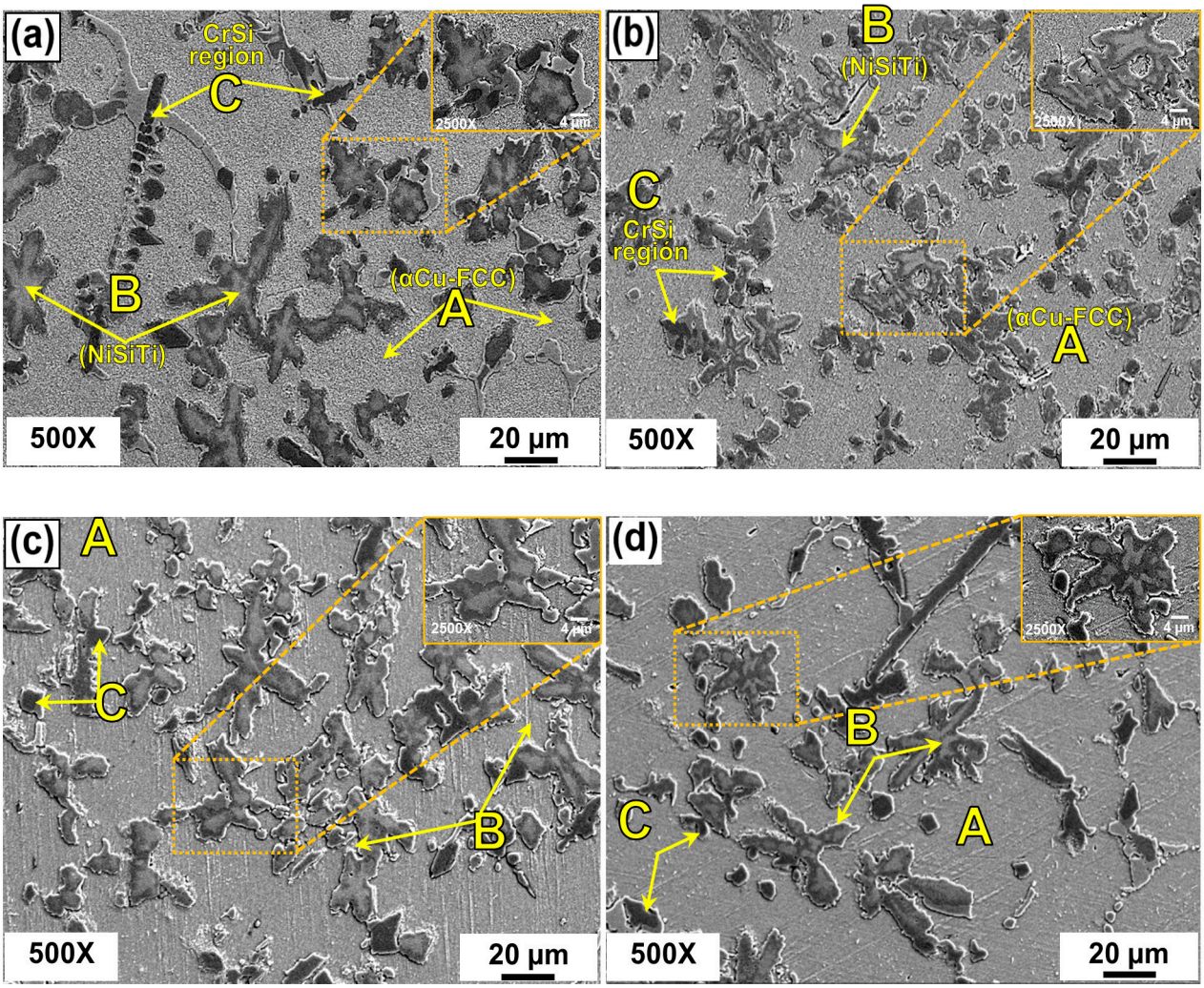

Figure 7. SEM micrographs of samples for M3 alloy: (**a**) E1; (**b**) E2; (**c**) E3; and (**d**) E4, respectively.

Figure 7b shows a microstructure containing a higher amount of dendritic phase B; which is directly related to the effect of the solubilizing heat treatment (ST). In contrast, Figure 7c shows a dendritic microstructure with a higher density and phase distribution, which is a product of microstructural evolution. Samples E3 and E4 contained more eutectic B and C phases, respectively. This is a product of the aging phenomenon, which is mainly caused by the temperature and time of aging. The following sections (see Figures 8–10) show the distribution of elements obtained by EDS elemental mapping of the different phases for alloys M1, M2, and M3 in the E1 condition.

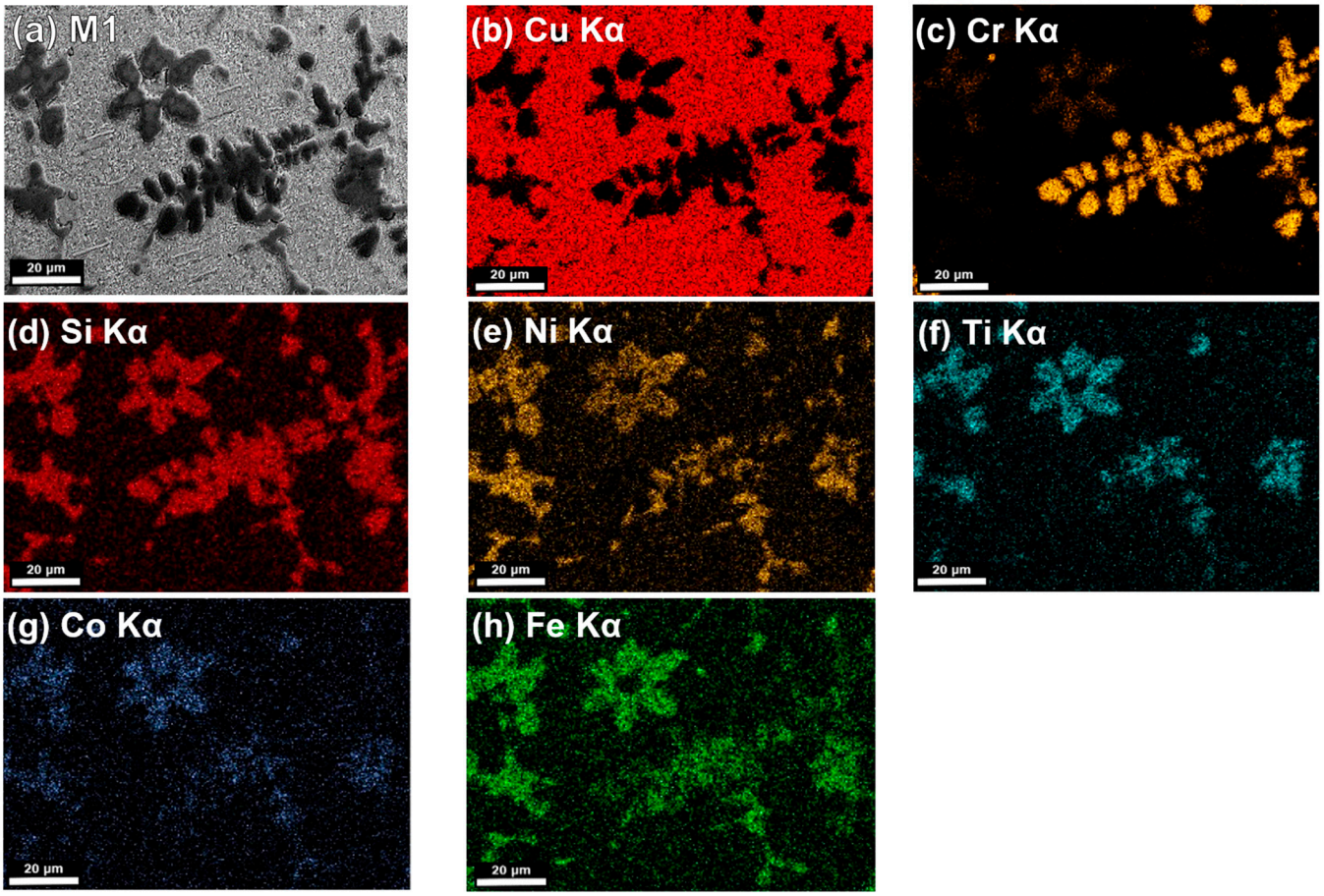

Figure 8. SEM-BSE image of (**a**) M1 alloy in as-cast condition (E1) and SEM-EDS elemental mapping images for (**b**) Cu Kα; (**c**) Si Kα; (**d**) Cr Kα; (**e**) Ni Kα; (**f**) Ti Kα; (**g**) Co Kα; and (**h**) Fe Kα from the same area as (**a**).

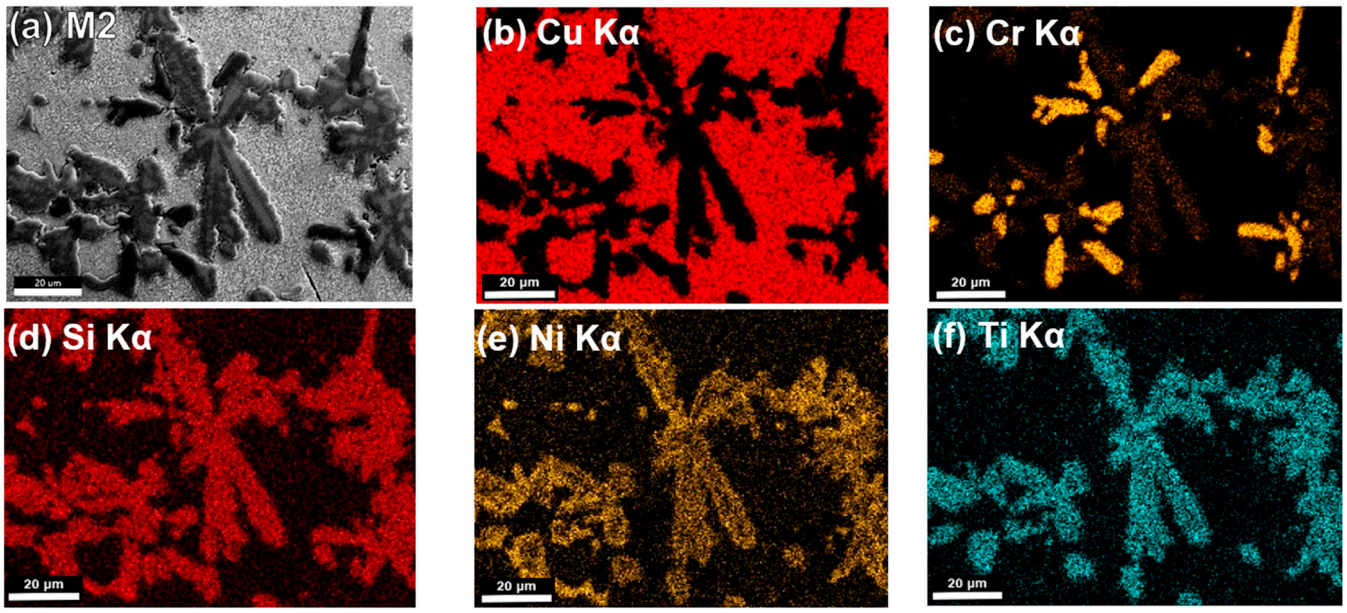

Figure 9. *Cont.*

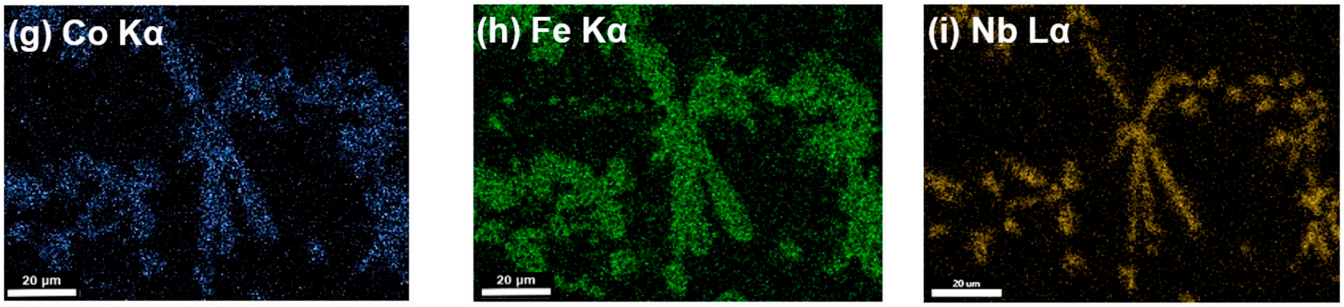

Figure 9. SEM-BSE image of (**a**) M2 alloy in as-cast condition (E1) and SEM-EDS elemental mapping images for (**b**) Cu Kα; (**c**) Si Kα; (**d**) Cr Kα; (**e**) Ni Kα; (**f**) Ti Kα; (**g**) Co Kα; (**h**) Fe Kα; and (**i**) Nb Kα from the same area as (**a**).

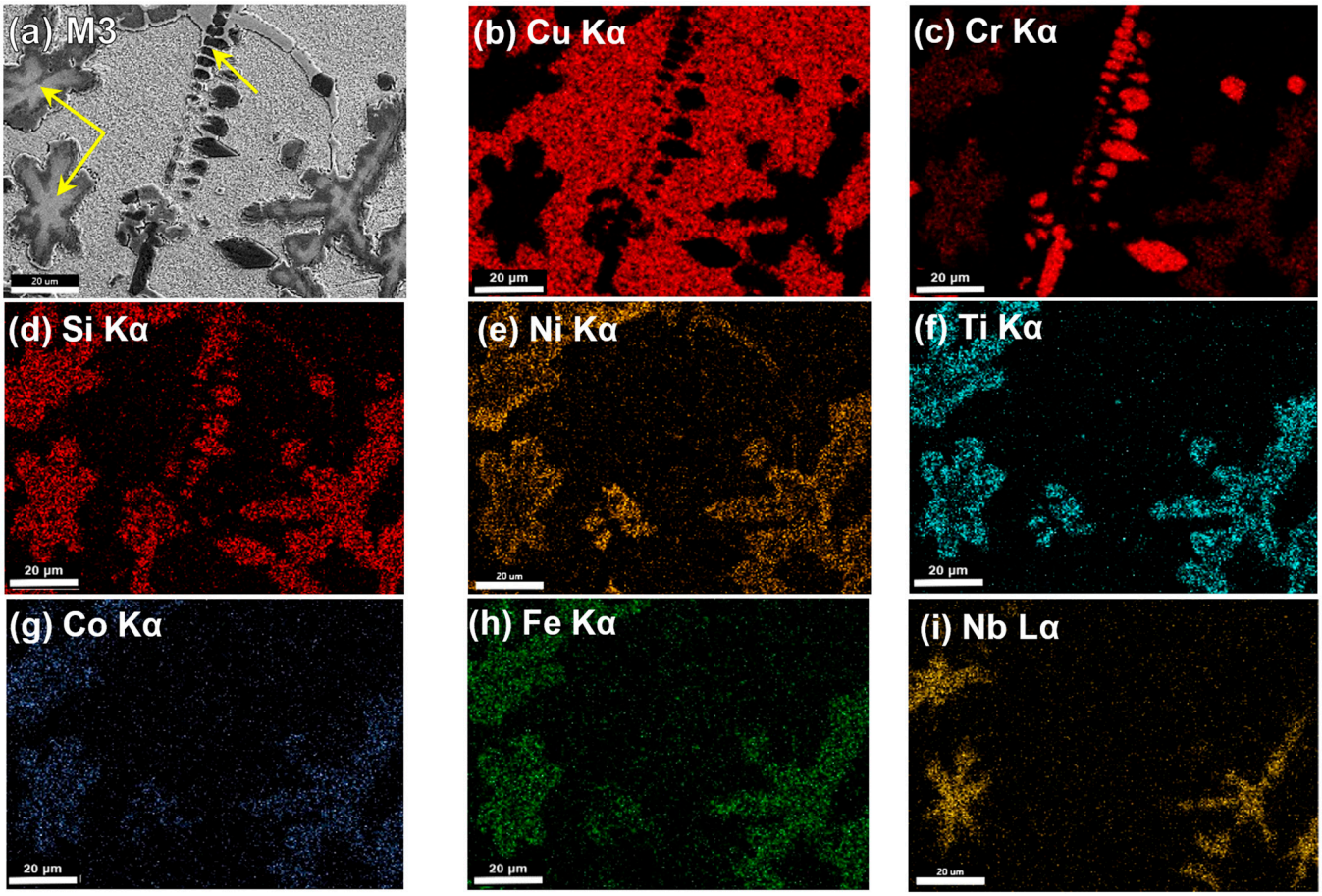

Figure 10. SEM-BSE image of (**a**) M3 alloy in as-cast condition (E1) and SEM-EDS elemental mapping images for (**b**) Cu Kα; (**c**) Si Kα; (**d**) Cr Kα; (**e**) Ni Kα; (**f**) Ti Kα; (**g**) Co Kα; (**h**) Fe Kα; and (**i**) Nb Kα from the same area as (**a**).

4.5. Elemental Distribution Analysis by SEM-EDS

Figure 8a shows a secondary electron image of alloy M1, and images (b–h) correspond to the elemental mapping for (b) Cu Kα, (c) Cr Kα, (d) Si Kα, (e) Ni Kα, (f) Ti Kα, (g) Co Kα, and (h) Fe Kα, respectively, in the same area as (a). Similarly, Figures 9 and 10 show the SEM-EDS elemental mapping for alloys M2 and M3, which includes the distribution of Nb in the figures labeled as (i). The figures reveal that phase A is predominantly Cu, phase B is composed of NiSiTi, and phase C is composed of CrSi. In Table 3, the average results of 10-point measurements of the EDS microanalysis performed on each phase are presented. As can be seen, Cu corresponds to 92.41 at% for average phase A. For phase

B, the average sum of NiSiTi was 49.46%, and for phase C, the average sum of CrSi was present at 93.60 at%; was is mainly composed of CrSi.

Table 3. The chemical composition for MEAs by EDS-SEM and average microhardness of individual phases in the as-cast condition.

Alloy	Phase	Elemental Constituents (at%)							
		Cu	Ni	Si	Cr	Co	Ti	Fe	Nb
M1	Nominal	73.00	5.50	6.10	11.40	1.00	2.40	0.60	0.00
	A	90.86	3.59	5.55	0.00	0.00	0.00	0.00	0.00
	B	32.08	24.12	23.35	4.71	2.94	5.43	7.37	0.00
	C	1.96	0.88	22.40	70.08	0.00	0.30	4.38	0.00
M2	Nominal	72.40	5.50	6.10	11.40	1.00	2.40	0.90	0.30
	A	95.45	2.87	5.68	0.00	0.00	0.00	0.00	0.00
	B	19.22	18.97	24.71	12.35	4.99	10.80	7.32	1.63
	C	2.37	0.78	22.82	69.74	0.69	0.71	2.88	0.00
M3	Nominal	71.80	5.50	6.10	11.40	1.00	2.40	1.20	0.60
	A	90.92	2.50	6.58	0.00	0.00	0.00	0.00	0.00
	B	4.59	9.79	25.55	19.29	7.20	5.67	8.83	19.08
	C	1.45	0.16	23.65	72.12	0.11	0.41	2.10	0.00

4.6. Hardness Rockwell B Results

Figure 11 shows the Rockwell hardness B (HRB) values for the experimental alloys M1, M2, and M3 in the cast condition (E1) and after solubilized heat treatment (E2) and aging for 30 and 60 min (E3 and E4).

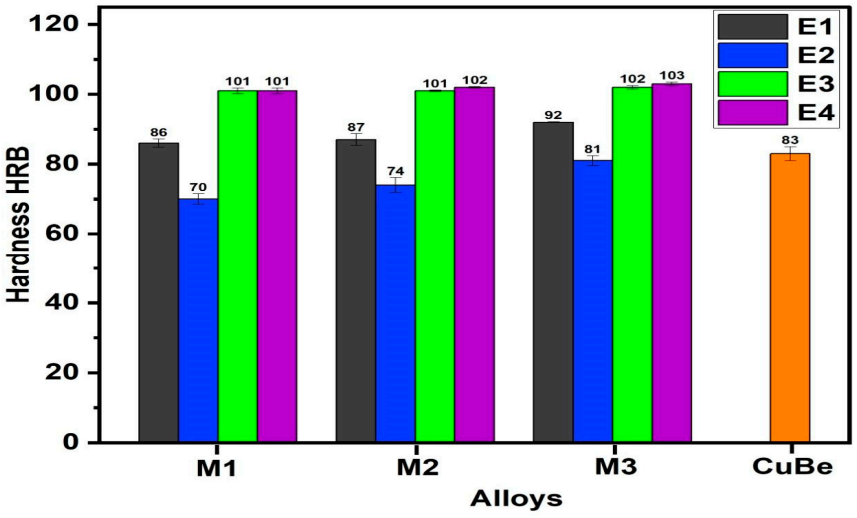

Figure 11. Hardness Rockwell B results for MEAs before (E1) and after heat treatments (E2, E3, and E4).

From Figure 11, it can be observed that the alloys in AC condition in the E1 samples with different Nb concentrations manifest a gradual increase in hardness values of 86 ± 1.21, 87 ± 1.70 and 92 ± 0.11 HRB for M1, M2, and M3, respectively. The gradual increase in hardness is attributed to the microstructural evolution caused by the Nb addition and the higher volume contents of the B and C phases. The samples in the ST condition (E2) exhibit reductions in hardness when compared to the E1 samples in the AC condition, with values of 70 ± 1.48, 74 ± 2.10 and 81 ± 1.40 HRB for alloys M1, M2, and M3. This decrease in hardness is due to a slight elemental reduction in the individual contents of the B and C

phases due to the migration and increased solubility of the alloying elements towards the A phase of the αCu matrix.

On the other hand, samples E3 and E4 in the ST condition at 30 and 60 min show similar behavior and a significant increase in hardness values compared to samples E1 and E2 in the AC and ST conditions, with values of 101 ± 0.8, 102 ± 0.2 and 103 ± 0.5 HRB, respectively, as well as M1, M2, and M3 under ET-60 conditions. The increase in hardness is attributed to the microstructural refinement and precipitation of Cr_3Si and Ni_2Si phases.

The hardness values of all entropy alloys are higher than those of the commercial CuBe alloy, which has a hardness value of 83 ± 2 HRB.

4.7. Vickers Hardness Results

The average Vickers microhardness (HV) values of phases A, B, and C of samples E1, E2, E3, and E4 of alloys M1, M2, and M3 are shown in Figure 12a. Indeed, the HV hardness results confirmed that the Cu-rich phase A had the lowest microhardness values, followed by the NiSiTi-rich phase B with intermediate values and the CrSi-rich phase C with the highest hardness values, with a minimum value of 815 HV in sample E1 and a maximum value of 1048 HV in sample E4. The changes in microhardness are predominantly influenced by the variation in the percentage content of each phase [see Figure 12b], their distribution, and the precipitation of particles that strength the αCu-FCC matrix during the aging heat treatment (AHT).

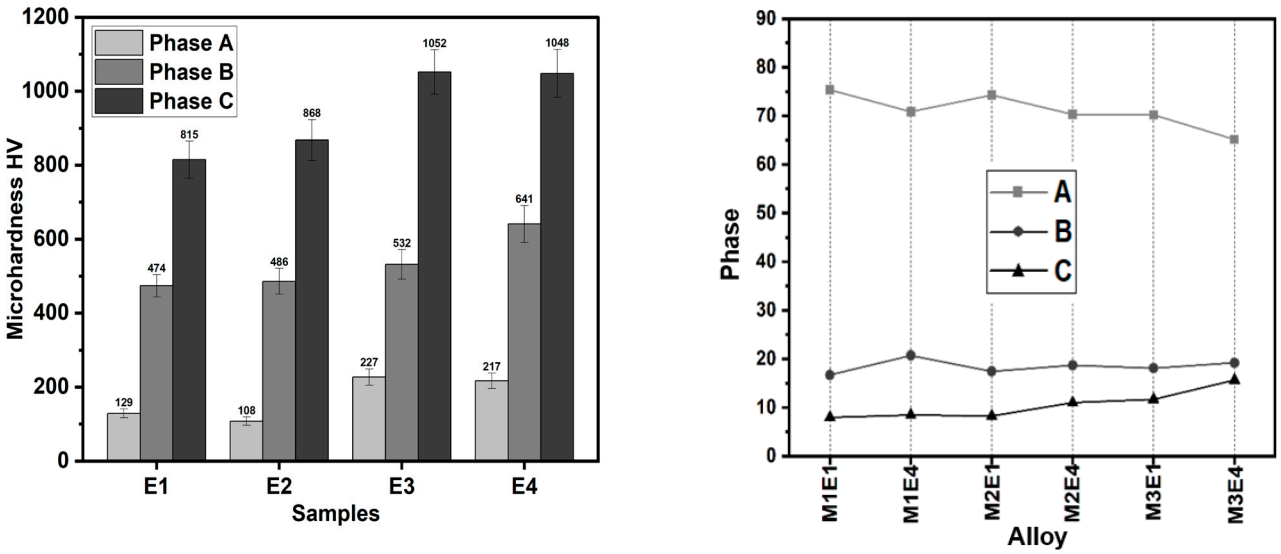

(**a**) (**b**)

Figure 12. Average HV microhardness of individual phases of alloys: (**a**) M1, M2, and M3 in AC (E1), ST (E2), ET-30 (E3), and ET-60 (E4) conditions; (**b**) Variation of the volumetric fraction of phases A, B and C in MEAs in state E1 and E4.

4.8. Friction and Wear Behaviors of the MEAs

Figures 13 and 14 show the friction and wear coefficient results of the different specimens for each alloy prior (E1) and after heat treatments (E2, E3, and E4), tested under a load of 30 N and over a total distance of 500 m, with continuous measurements every 125 m, using a ball-on-disc tribometer, without lubrication, and at room temperature.

From the results obtained, it is important to emphasize that all the E1 samples presented the highest coefficient of friction (see Figure 14), but the behavior of the coefficient of friction after 125 m was stable; this was similar for all M1, M2, and M3 alloy samples.

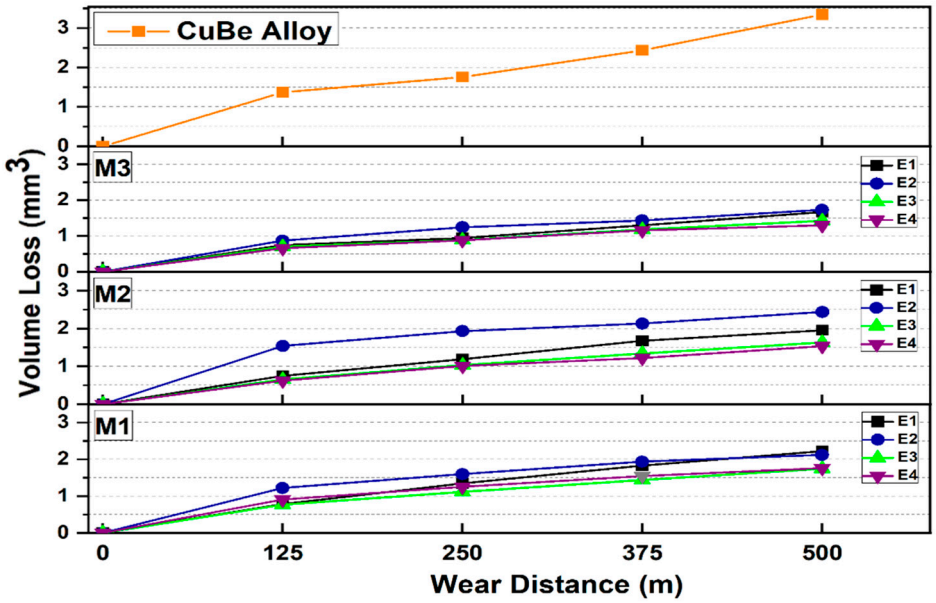

Figure 13. Wear volumes of disc samples for M1, M2, and M3 alloys before (E1) and after heat treatments (E2, E3, E4); and for CuBe commercial alloy.

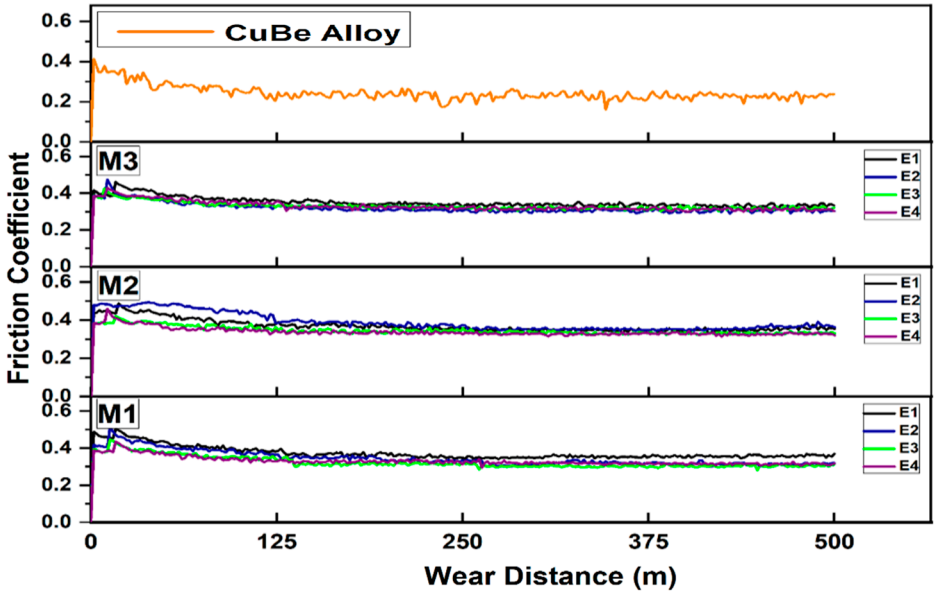

Figure 14. The friction coefficient versus wear distance at the surface of M1, M2, and M3 alloys before (E1) and after heat treatments (E2, E3, E4); and for CuBe commercial alloy.

On the other hand, from the E1 samples in the casting condition, it can be seen that the wear resistance results (see Figure 13) experienced a gradual decrease in volume loss as the Nb content increased, resulting in a stepwise behavior of volume loss of 2.22 mm^3, 1.95 mm^3, and 1.67 mm^3 for the M1, M2, and M3 alloys (see Figure 16). This behavior can be attributed to the gradual decrease in the average surface roughness values (0.056 µm for M1, 0.052 µm for M2, and 0.047 µm for M3) and strengthening of the microstructure caused by Nb addition.

Compared to the E1 specimens in the casting condition, it can be seen that all E3 and E4 specimens subjected to thermal aging treatment at 30 and 60 min had the lowest values of the coefficient of friction, obtaining better stability after a sliding distance of 125 m (Figure 14). In this sense, it has been proven that aging heat treatment helps improve wear resistance. The wear values for the E3 specimens in the ET-30 condition showed a

reduction in wear volume loss of 1.75 mm^3, 1.63 mm^3, and 1.42 mm^3 for M1, M2, and M3, respectively. On the other hand, the E4 specimens in the ET-60 condition showed similar behavior to the E3 specimens in the ET-30 condition.

This behavior is explained in terms of the strengthening properties resulting from the refinement of the microstructure and the distribution of dispersed precipitates in the αCu matrix and interdendritic boundaries. Nb additions increase phases B and C and improve their distribution, as explained in Section 4.2.

The best results were obtained for sample E3 (1.42 mm^3) of M3 alloy and sample E4 (1.29 mm^3). Comparatively, the CuBe C17510 alloy exhibited a material loss of 3.34 mm^3.

Figures 13 and 14 show the friction and wear coefficient results of the different specimens for each alloy before (E1) and after heat treatments (E2, E3, and E4), tested under a load of 30 N and over a total distance of 500 m, with continuous measurements every 125 m, using a ball-on-disc tribometer, without lubrication, and at ambient temperature.

Figure 15a–d show a series of SEM-SEI images obtained from the abraded surfaces of alloys M1, M2, M3, and the commercial CuBe alloy. As seen in the images labeled a, b, and c for alloys M1, M2, and M3, respectively, there is less surface damage with increasing Nb addition. Therefore, it can be seen that alloy M1 has the highest superficial damage compared to alloys M2 and M3. Similarly, the commercial alloy CuBe exhibited significant surface damage on the wear surface [Figure 15d] and in the isometrics and cross-sectional profiles [Figure 16d].

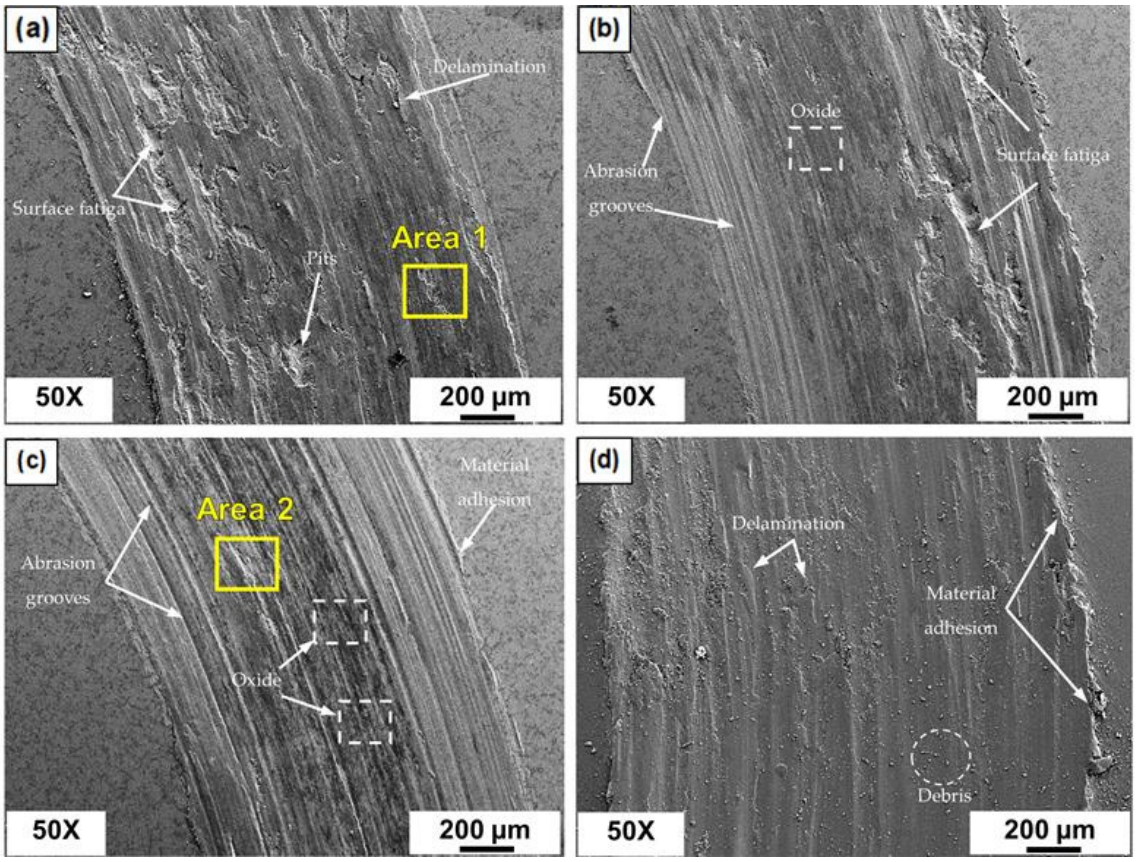

Figure 15. SEM images (SEI) obtained after the wear test at a sliding distance of 500 m on the worn surfaces of the (**a**) M1; (**b**) M2; and (**c**) M3 alloy in as-cast condition (E1) and (**d**) CuBe commercial alloy, respectively.

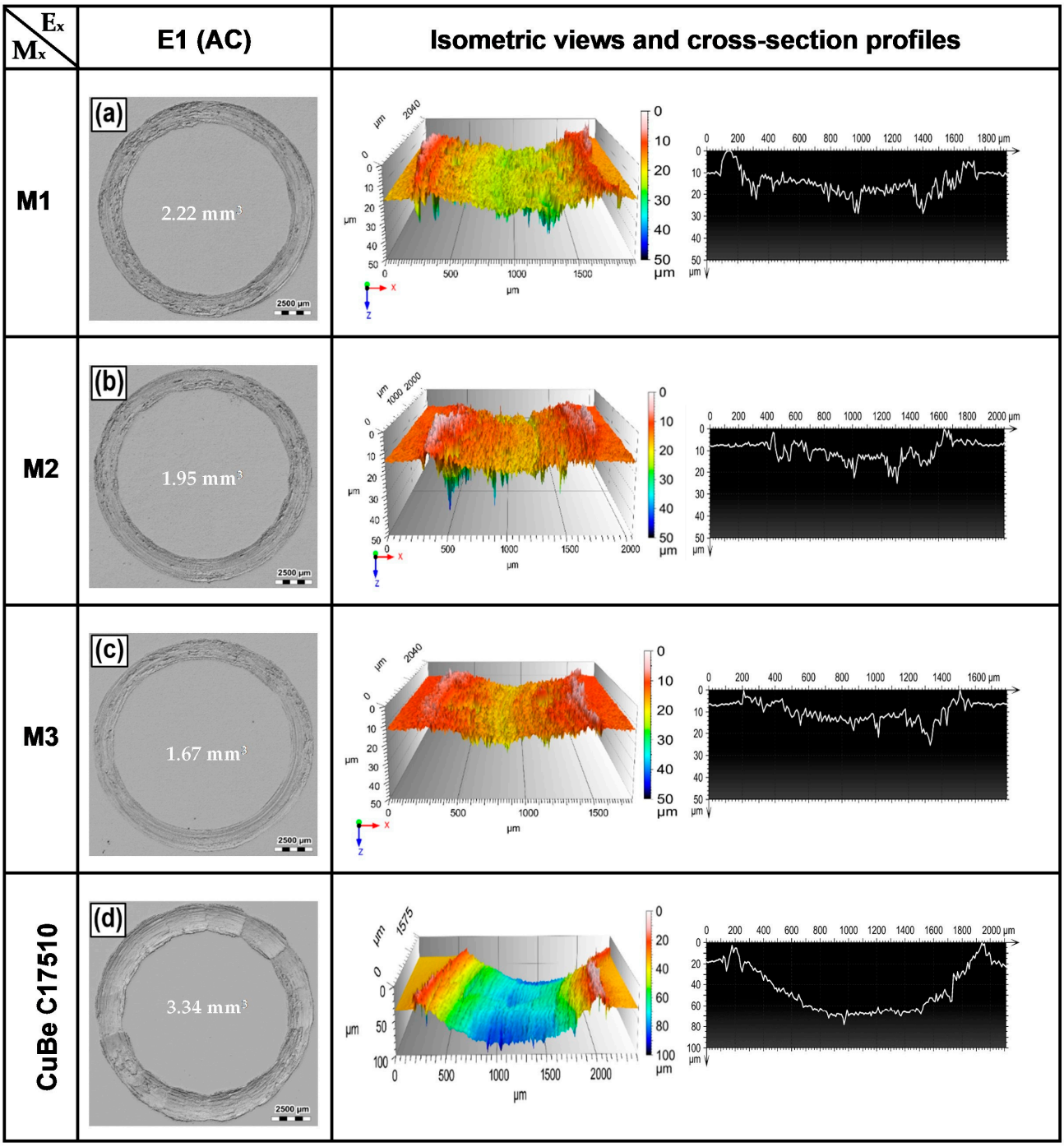

Figure 16. Isometric views and cross-section profiles obtained after the wear test at a sliding distance of 500 m and at a normal force of 30 N on the worn surfaces of the (**a**,**c**) M3 alloy in as-cast condition (E1) and (**b**,**d**) CuBe commercial alloy.

The M1 alloy and the commercial alloy CuBe C17510 exhibited the most significant levels of deformation and wear damage. The main wear mechanisms observed in the images shown in Figure 15 are mainly caused by the detachment of hard abrasive particles (debris), leading to a transition in the wear mechanism from sliding to abrasive wear. This causes severe damage, such as abrasive grooves, surface fatigue, and pits owing to plastic deformation.

A sequence of 3D images digitized with a non-contact optical profilometer is shown in Figure 16, resulting in the surface morphology of the wear trace and the corresponding cross-sectional profile for each sample. By comparing the worn surface traces of alloys

(a) M1, (b) M2, and (c) M3 in casting condition E1 and (d) the commercial alloy CuBe C17510, it is evident that alloy M3 shows less damage compared to alloys M2 and M1. In addition, it is observed that the CuBe alloy sample was the one that, under the same test conditions, experienced a greater increase in the width of the wear trace and, consequently, a more significant loss of material.

The SEM-SEI and SEM-EDS elemental mapping images in Figure 17 show the oxide layers formed on the surfaces of alloys (a) M1 and (b) M3, which are listed in Figure 15 as Areas 1 and 2. As discussed, the greater number of high-hardness particles within the soft and ductile matrix caused more surface damage and discontinuity in the oxide layer, resulting in more Cu alloy/steel ball contact. A stable and present oxide layer is essential for minimizing and stabilizing the friction coefficient, which helps reduce direct metal-to-metal contact and wear losses.

The M3 alloy experienced the least surface damage owing to ductile deformation, which can also be attributed to the formation of oxide incrustations that protect and provide greater smoothness and stability to the surface, thus benefiting wear resistance. Previous studies have reported the effect of Ti and the formation of oxides that provide greater protection and surface stability, thus improving the resistance to sliding wear [25,26].

The wear particles (debris) captured in the SEM-BSE micrographs in Figure 18 were obtained after performing the wear tests at a distance of 500 m with a regular load of 30 N. The SEM micrographs show that the particles collected from the E1 specimen of alloys M1 and M2 are larger than the E1 specimen of alloy M3. The SEM micrographs show that the particles collected from E1 specimens of alloys M1 and M2 were larger than those from E1 specimens of Alloy M3. However, due to its wear mechanism, the commercial alloy CuBe had the largest particle size. In addition, the EDS microanalysis of the same area in Figure 18 is shown.

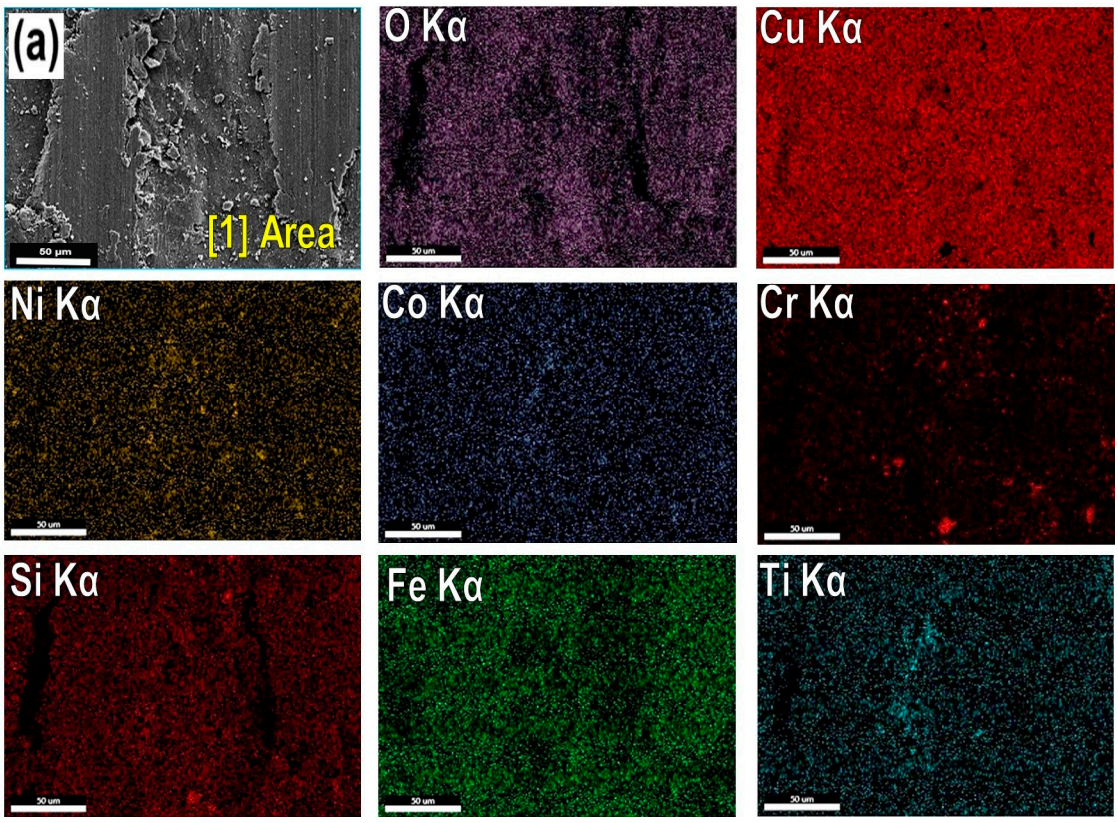

Figure 17. *Cont.*

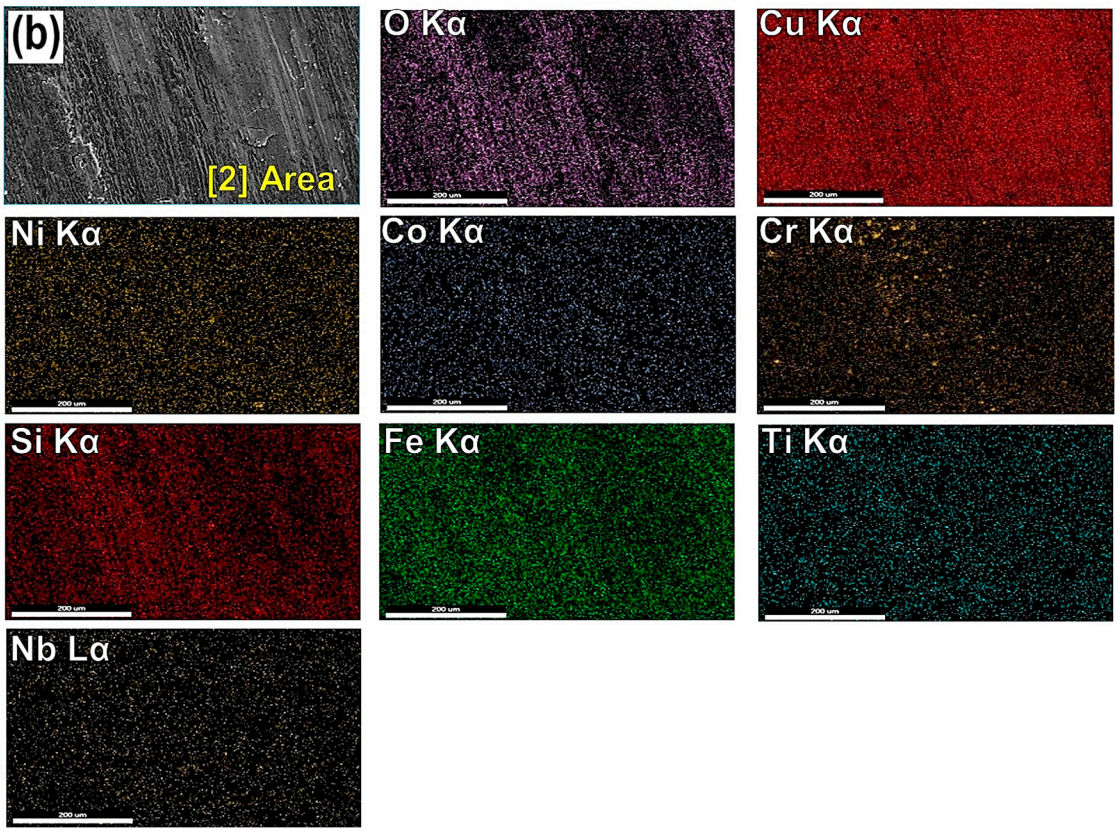

Figure 17. SEM images of wear marks and SEM-EDS elemental mapping images of oxide scale formed on Area 1 of (**a**) M1 alloy and Area 2 of (**b**) M3 after the wear test from the same area marked in Figure 15a,c.

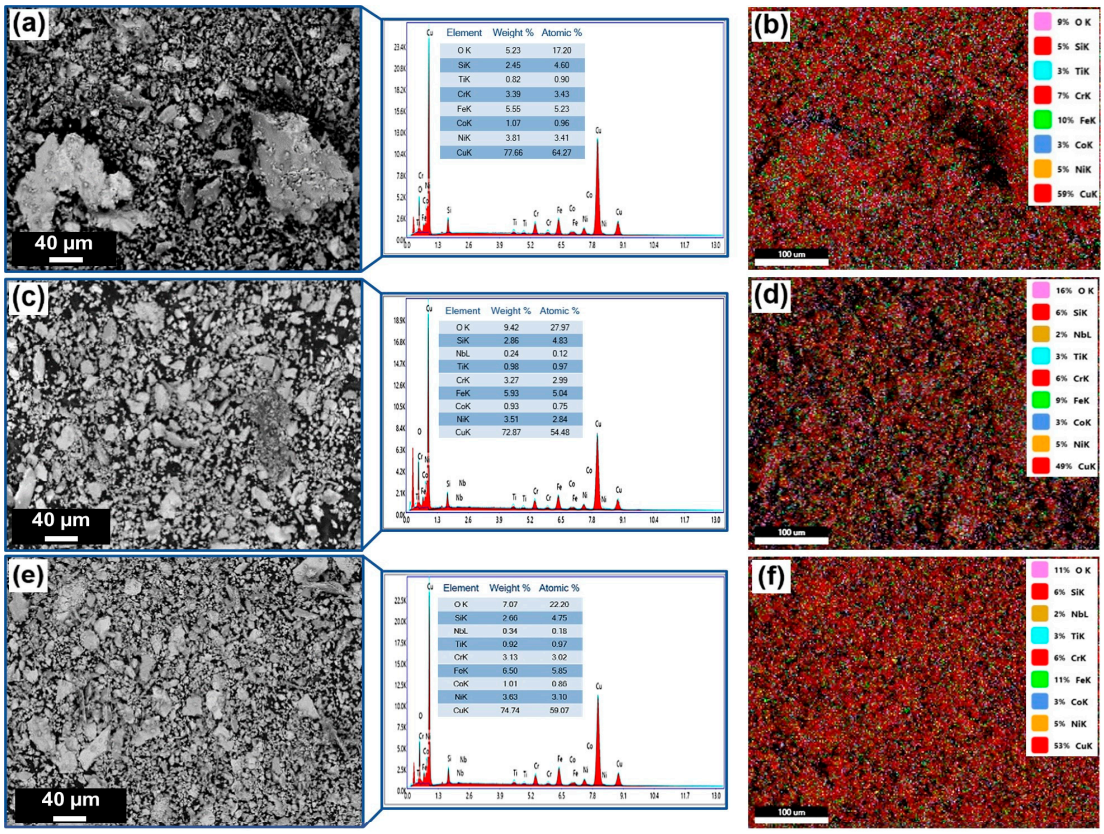

Figure 18. *Cont.*

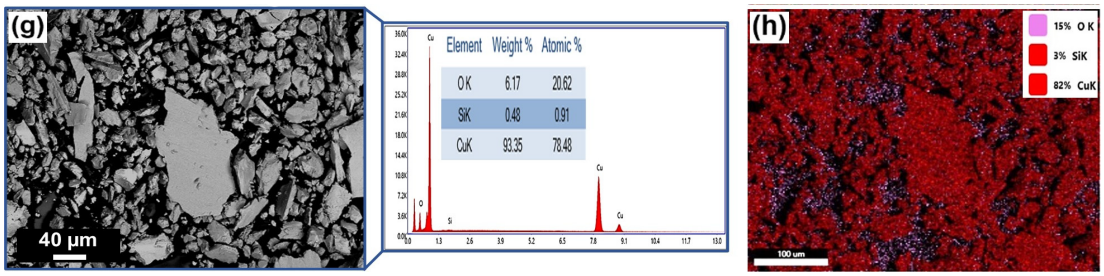

Figure 18. SEM micrographs and EDS mapping-Spectrum area of the wear debris collected from the samples in as-cast condition (E1): (**a**,**b**) M1; (**c**,**d**) M2; (**e**,**f**) M3; and (**g**,**h**) CuBe alloy.

5. Conclusions

In this study, the impacts of Nb addition and heat treatment on the phase transformation, structural properties, material strength, and durability of medium entropy copper-based alloys (MEAs) were investigated, as well as the commercial alloy CuBe C17510 for comparison. The conclusions are as follows.

(1) Nb additions were found to favor the gradual increase in configurational entropy values of 8.17 J/mol-K for M1, 8.38 J/mol-K for M2 and 8.61 J/mol-K for M3, which favors the formation of solid solutions and crystalline structures of BCC and FCC types.

(2) The XRD and SEM-EDS spectra showed that the medium-entropy alloys were mainly composed of the FCC phase (αCu) and the precipitated phases Co_2Nb, Ni_2Si and Cr_3Si. In addition, the XRD spectra revealed that the (111) peak undergoes an important variation in the diffraction angle, with a slight shift to larger angles of 50.64°, 50.65°, and 50.69° with an increase in Nb content, which causes at the decrease in lattice parameters in M1, M2, and M3, respectively.

(3) Nb addition and heat treatments strengthened the microstructure through the refinement and distribution of the precipitated phases.

(4) The high hardness values of the as-cast samples manifested a gradual increase of 86 ± 1.21, 87 ± 1.70 and 92 ± 0.11 HRB for M1, M2, and M3, respectively. This increase in hardness is attributed to the microstructural evolution caused by the addition of Nb. In addition, the hardness values of the aged samples were higher than those of the as-cast and commercial CuBe C17510 alloy.

(5) The wear behavior analysis revealed that the E1 samples in as-cast condition obtained satisfactory wear resistance results as the Nb content increased, resulting in a stepwise lost volume behavior of 2.22 mm^3, 1.95 mm^3 and 1.67 mm^3 for the M1, M2, and M3 alloys. On the other hand, wear values for the E4 samples in TTE-60 aged condition reflected a reduction in material loss of 1.77 mm^3, 1.53 mm^3, and 1.29 mm^3 for M1, M2, and M3. For the CuBe alloy C17510, the material loss was 3.34 mm^3.

Author Contributions: Conceptualization, D.A.A.-S. and A.J.-H.; methodology, D.A.A.-S. and A.J.-H.; software, D.A.A.-S.; validation, D.A.A.-S. and A.J.-H.; formal analysis, D.A.A.-S. and N.J.I.-B.; investigation, D.A.A.-S.; resources, A.J.-H. and J.M.T.; data curation, J.M.T.; writing—original draft preparation, D.A.A.-S. and J.L.C.-M.; writing—review and editing, D.A.A.-S., A.J.-H. and J.M.T.; supervision, A.J.-H.; project administration, D.A.A.-S. and A.J.-H. All authors have read and agreed to the published version of the manuscript.

Funding: This research was funded by CONACYT-México and Altea Casting S.A de C.V. This article was published with the financial support of the Directorate of Scientific, Humanistic and Technological Research (DICIHT) of the National Autonomous University of Honduras.

Data Availability Statement: The original data used to support the findings of this study are available from the corresponding author upon request.

Acknowledgments: This work was supported by Universidad Autónoma de Nuevo León, CONACYT, and Altea Casting S.A de C.V. Author Denis Ariel Avila Salgado is grateful to CONACYT, México, for the doctoral scholarship and the National Autonomous University of Honduras for their complementary support throughout the research process.

Conflicts of Interest: The authors declare no conflict of interest.

References

1. Ma, L.; Zhao, D.; Wang, Y.; Wang, K.; Huang, J.; Jin, X.; Kong, D.; Wang, M.; Yamaguchi, T.; Wang, H. Optimized Wear Behaviors and Related Wear Mechanisms of Medium Entropy Alloy-Based Composite Coatings. *J. Mater. Res. Technol.* **2024**, *29*, 12–27. [CrossRef]
2. Wu, J.; Ren, D.; Xie, B.; He, R.; Geng, Z.; Zhang, Z.; Liu, Y.; Wang, D.; Zhu, Y.; Zhang, W. Effect of Cr_3C_2 Addition on Microstructure and Mechanical Properties of WC-CoNiFe Cemented Carbides. *Metals* **2024**, *14*, 895. [CrossRef]
3. Avila-Salgado, D.A.; Juárez-Hernández, A.; Lara Banda, M.; Bedolla-Jacuinde, A.; Guerra, F.V. Effects of Nb Additions and Heat Treatments on the Microstructure, Hardness and Wear Resistance of CuNiCrSiCoTiNbx High-Entropy Alloys. *Entropy* **2022**, *24*, 1195. [CrossRef]
4. Chang, H.; Wang, S.; Mao, Z.; Zhang, T.; Li, Z.; Wang, Z. Influence of Si Addition on the Microstructures, Phase Assemblages and Properties in CoCrNi Medium-Entropy Alloy. *Materials* **2024**, *17*, 2893. [CrossRef]
5. Avila-Salgado, D.A.; Juárez-Hernández, A.; Cabral-Miramontes, J.; Camacho-Martínez, J.L. Strengthening Properties and Wear Resistance of the Cu-xNi-yCo-Cr-Si Alloy by Varying Ni/Co and Zr Addition. *Lubricants* **2021**, *9*, 96. [CrossRef]
6. VOSviewer—Visualizing Scientific Landscapes. Available online: https://www.vosviewer.com// (accessed on 29 June 2024).
7. Zhou, L.; Liu, H.; Zhang, Q.; Liang, J.; Peng, Y.; Hao, X.; Yang, C.; Liu, Y.; Wang, Y. Effect of Al/Cu Ratio on Microstructure and High-Temperature Oxidation Resistance of AlxCoCrCuyFeNi High-Entropy Alloy Coatings. *J. Manuf. Mater. Process.* **2025**, *9*, 13. [CrossRef]
8. Yang, Z.; Chen, W.; Hao, L.; Chu, C.; Zeng, D.; Xiong, W.; Fu, Z. Microstructure and Mechanical Properties of As-Cast (CuNi)100−xCox Medium-Entropy Alloys. *China Foundry* **2022**, *19*, 511–518. [CrossRef]
9. Du, Y.; Pei, X.; Tang, Z.; Zhang, F.; Zhou, Q.; Wang, H.; Liu, W. Mechanical and Tribological Performance of CoCrNiHf*x* Eutectic Medium-Entropy Alloys. *J. Mater. Sci. Technol.* **2021**, *90*, 194–204. [CrossRef]
10. Wang, W.; Chen, Z.; Guo, E.; Zhang, S.; Kang, H.; Wang, T. Effects of Cr Addition on the Precipitation and Properties of Cryo-Rolled CuNiSi Alloys. *Metals* **2023**, *13*, 758. [CrossRef]
11. Wang, J.; Gao, J.; Yang, H.; Yang, F.; Wen, T.; Liu, Z.; Zhang, L.; Ji, S. High-Strength Al–5Mg2Si–2Mg–2Fe Alloy with Extremely High Fe Content for Green Industrial Application through Additive Manufacturing. *Virtual Phys. Prototyp.* **2023**, *18*, e2235587. [CrossRef]
12. Zhao, Y.; Ma, W.; Tisov, O. Enhancing Reciprocating Wear Resistance of Co37Cr28Ni31Al2Ti2 Spark Plasma Sintered Medium-Entropy Alloy via TiC Addition. *Materials* **2025**, *18*, 442. [CrossRef]
13. Wang, T.; Zhang, J.; Zhang, Y.; Chen, S.; Luo, Z.; Wu, J.; Zhu, L.; Lei, J. Improving Wear and Corrosion Resistance of LDEDed CrFeNi MEA through Addition of B and Si. *J. Alloys Compd.* **2023**, *968*, 172223. [CrossRef]
14. Rahimi, E.; Rezayat, M.; Mahdavi, S. Enhancing Wear Resistance of CoNiCrMo Medium Entropy Alloy through Cold Working and Aging: Tradeoffs with Corrosion Performance. *J. Mater. Res. Technol.* **2024**, *33*, 6890–6901. [CrossRef]
15. Zhou, E.; Qiao, D.; Yang, Y.; Xu, D.; Lu, Y.; Wang, J.; Smith, J.A.; Li, H.; Zhao, H.; Liaw, P.K.; et al. A Novel Cu-Bearing High-Entropy Alloy with Significant Antibacterial Behavior against Corrosive Marine Biofilms. *J. Mater. Sci. Technol.* **2020**, *46*, 201–210. [CrossRef]
16. Ren, G.; Huang, L.; Hu, K.; Li, T.; Lu, Y.; Qiao, D.; Zhang, H.; Xu, D.; Wang, T.; Li, T.; et al. Enhanced Antibacterial Behavior of a Novel Cu-Bearing High-Entropy Alloy. *J. Mater. Sci. Technol.* **2022**, *117*, 158–166. [CrossRef]
17. Chen, C.; Chen, J.; Yuan, S.; Li, W.; Wang, W.; Li, X.; Zhang, W.; Wei, R.; Guan, S.; Wang, T.; et al. Microstructure, Mechanical Properties, Corrosion Resistance and Anti-Bacterial Behavior of Novel Co-Free High Entropy Alloys. *J. Alloys Compd.* **2022**, *902*, 163714. [CrossRef]
18. *ASTM G99-05(2010)*; Standard Test Method for Wear Testing with a Pin-on-Disk Apparatus. ASTM International: West Conshohocken, PA, USA, 2011. [CrossRef]
19. Zhang, Y.; Zhou, Y.J.; Lin, J.P.; Chen, G.L.; Liaw, P.K. Solid-Solution Phase Formation Rules for Multi-Component Alloys. *Adv. Eng. Mater.* **2008**, *10*, 534–538.
20. Guo, S.; Liu, C.T. Phase Stability in High Entropy Alloys: Formation of Solid-Solution Phase or Amorphous Phase. *Prog. Nat. Sci. Mater. Int.* **2011**, *21*, 433–446.
21. Yang, X.; Zhang, Y. Prediction of High-Entropy Stabilized Solid-Solution in Multi-Component Alloys. *Mater. Chem. Phys.* **2012**, *132*, 233–238.

22. Guo, S.; Ng, C.; Lu, J.; Liu, C.T.; Carlo, M.; Guo, S.; Ng, C.; Lu, J.; Liu, C.T. Effect of Valence Electron Concentration on Stability of Fcc or Bcc Phase in High Entropy Alloys Effect of Valence Electron Concentration on Stability of Fcc or Bcc Phase in High Entropy Alloys. *J. Appl. Phys.* **2011**, *109*, 103505.
23. Nong, Z.S.; Zhu, J.C.; Cao, Y.; Yang, X.W.; Lai, Z.H.; Liu, Y. Stability and Structure Prediction of Cubic Phase in as Cast High Entropy Alloys. *Mater. Sci. Technol. U. K.* **2014**, *30*, 363–369. [CrossRef]
24. *ASTM 407-07*; Standard Practice for Microetching Metals and Alloys. ASTM International: West Conshohocken, PA, USA, 2007; pp. 1–21. [CrossRef]
25. Erdogan, A.; Doleker, K.M.; Zeytin, S. Effect of Al nd Ti on High-Temperature Oxidation Behavior of CoCrFeNi-Based High-Entropy Alloys. *Jom* **2019**, *71*, 3499–3510. [CrossRef]
26. Xu, Z.; Li, D.Y.; Chen, D.L. Effect of Ti on the wear behavior of AlCoCrFeNi high-entropy alloy during unidirectional and bi-directional sliding wear processes. *Wear* **2021**, *476*, 203650. [CrossRef]

Disclaimer/Publisher's Note: The statements, opinions and data contained in all publications are solely those of the individual author(s) and contributor(s) and not of MDPI and/or the editor(s). MDPI and/or the editor(s) disclaim responsibility for any injury to people or property resulting from any ideas, methods, instructions or products referred to in the content.